JACS
JOURNAL OF THE AMERICAN CHEMICAL SOCIETY
Article
Cite This: J. Am. Chem. Soc. 2018, 140, 6249−6259
pubs.acs.org/JACS

Experimental and Theoretical Structural Investigation of AuPt Nanoparticles Synthesized Using a Direct Electrochemical Method

Aliya S. Lapp,[†,‡] Zhiyao Duan,[†,§] Nicholas Marcella,[∥] Long Luo,[†,‡,#] Arda Genc,[⊥] Jan Ringnalda,[⊥] Anatoly I. Frenkel,*[,∥] Graeme Henkelman,*[,†,§] and Richard M. Crooks*[,†,‡]

[†]Department of Chemistry, [‡]Texas Materials Institute, and [§]Institute for Computational and Engineering Sciences, The University of Texas at Austin, 2506 Speedway, Stop A5300, Austin, Texas 78712-1224, United States

[∥]Department of Materials Science and Chemical Engineering, Stony Brook University, Stony Brook, New York 11794, United States

[⊥]Thermo Fisher Scientific, 5350 NE Dawson Creek Drive, Hillsboro, Oregon 97124, United States

Supporting Information

ABSTRACT: In this report, we examine the structure of bimetallic nanomaterials prepared by an electrochemical approach known as hydride-terminated (HT) electrodeposition. It has been shown previously that this method can lead to deposition of a single Pt monolayer on bulk-phase Au surfaces. Specifically, under appropriate electrochemical conditions and using a solution containing $PtCl_4^{2-}$, a monolayer of Pt atoms electrodeposits onto bulk-phase Au immediately followed by a monolayer of H atoms. The H atom capping layer prevents deposition of Pt multilayers. We applied this method to ∼1.6 nm Au nanoparticles (AuNPs) immobilized on an inert electrode surface. In contrast to the well-defined, segregated Au/Pt structure of the bulk-phase surface, we observe that HT electrodeposition leads to the formation of AuPt quasi-random alloy NPs rather than the core@shell structure anticipated from earlier reports relating to deposition onto bulk phases. The results provide a good example of how the phase behavior of macro materials does not always translate to the nano world. A key component of this study was the structure determination of the AuPt NPs, which required a combination of electrochemical methods, electron microscopy, X-ray absorption spectroscopy, and theory (DFT and MD).

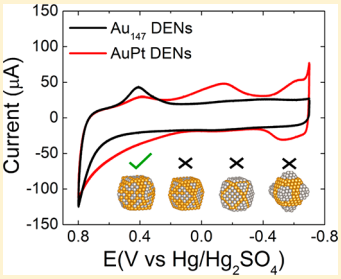

INTRODUCTION

Pt is an important catalyst for many reactions, but it is expensive and hence there is a strong motivation for reducing its usage.[1] One strategy for minimizing the need for Pt, yet retaining its desirable catalytic properties, is to form atomically thin Pt layers on more abundant, less expensive materials.[1−4] One might imagine this could be accomplished by direct deposition of Pt, but that approach can lead to three-dimensional growth (rather than stopping at a single monolayer (ML)).[5,6] In recent years, however, new methods have been discovered that are much more effective for depositing Pt ML and controlled multilayer films onto underlying metals.

One of the most intriguing methods for controlled deposition of Pt was recently reported by Moffat and co-workers.[7−9] Specifically, they showed that close to a single Pt ML can be deposited onto a macroscopic Au surface using a hydride-termination (HT) process (Scheme 1).[7,8] In this approach, the potential of an Au electrode is pulsed to a value that sequentially deposits Pt and then adsorbed H atoms (H_{ads}) atop the newly deposited Pt atoms. The presence of H_{ads} prevents three-dimensional growth of Pt multilayers.[7] Finally, the potential is pulsed positive to remove H_{ads}. Repetition of steps 2 and 3 (Scheme 1) can be used to deposit up to 10 Pt layers,[7,8] although iterations 2−10 do not necessarily result in complete additional MLs.[8,10]

Scheme 1

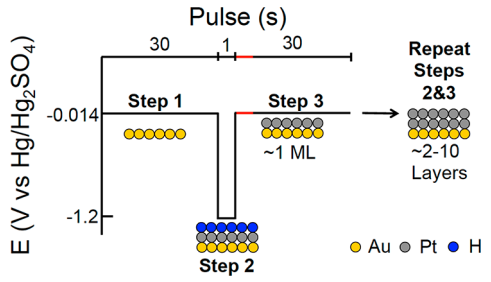

Following the original study of the HT method,[7] related self-terminating electrodeposition[6,9,11−17] and chemical deposition[1,18] methods were reported. For example, Behm and co-workers[6] demonstrated that CO_{ads} could replace H_{ads} as the capping agent for Pt, and Vanpaemel and co-workers[11] reported that ultrathin Ni films could be deposited onto TiN. The HT method has also been adapted for Pt deposition onto: Ni,[9] star-shaped dendritic Au nanorods,[19] and carbon fiber substrates;[20,21] Ir deposition on Au, Pt, and Ni;[14] and for PtCoNi alloy formation.[13] To the best of our knowledge,

Received: November 21, 2017
Published: May 11, 2018

DOI: 10.1021/jacs.7b12306
J. Am. Chem. Soc. 2018, 140, 6249−6259

however, the efficacy of this method has not been tested for ML shell deposition onto nanoparticles (NPs).

In this Article, therefore, we report in-depth characterization of NPs prepared by the HT method, and specifically Pt deposition onto ∼1−2 nm AuNP cores. The Au cores were prepared by a dendrimer templating method we[3,22−25] and others[26−28] have described previously. On the basis of the original reports of HT Pt deposition onto bulk materials,[7−9] we anticipated that Pt deposition onto AuNPs would yield Au@Pt core@shell structures. However, the results of extensive structural characterization suggest the resulting materials more closely resemble quasi-random alloys.

The results described here are interesting for two primary reasons. First, the HT method could be very useful for preparing, for example, catalytic NPs, but its extension from bulk to NP surfaces is not a foregone conclusion. This is because the geometric and electronic properties of the surfaces of 1−2 nm NPs, such as those used here, are very different from those of bulk surfaces.[3,29,30] Successful application of the HT method to NPs has the potential to greatly expand the scope of the HT-deposition approach.[7−9,13,14]

Second, the HT method for NPs could be more versatile than the most common method used for depositing ML shells of metals onto small cores: underpotential deposition (UPD) followed by galvanic exchange (GE).[2,31,32−35,36−41] UPD is an electrochemical method that provides a means for depositing a single ML of a shell metal (e.g., Cu) onto a core at a potential more positive than that of the onset for bulk metal deposition.[40] Once deposited, the UPD metal can be galvanically exchanged for a second, more noble metal (e.g., Pt). There are some significant limitations of the UPD/GE approach, however. For example, the preparation of multiple, discrete ML shells using combined UPD/GE is challenging and can result in alloying between the UPD and final shell metals if exchange is incomplete.[16,41−44] For catalysis this is important, because as we have shown, even a few heteroatoms can dramatically change the catalytic properties of NPs.[43] Additionally, the UPD/GE method is limited to shell metals more noble than the UPD metal.[39] The HT method directly addresses these types of problems and limitations.

For this Article, we chose to study Au@Pt NPs in part because this was the same combination of metals used in the original report of the HT method on bulk surfaces.[7] Also, we have previously synthesized Au@Pt NPs using either Cu[34] or Pb[35,36] UPD followed by GE with Pt^{2+}, and therefore have direct experience with this alternative synthetic method. The results presented here show that the HT method does lead to deposition of Pt on ∼1.6 nm AuNPs, but that the resulting structure is more consistent with that of a quasi-random alloy than a simple core@shell model. We reached this conclusion by combining data from electrochemical measurements, electron microscopy, X-ray absorption spectroscopy, and theory. The main conclusion of this work, that alloying occurs in NPs using the HT method, is in contrast to the segregation of the two metals observed in bulk phase, and it provides a good example of how the phase behavior of macro materials does not always translate to the nano world.

EXPERIMENTAL SECTION

Chemicals and Materials. Sixth-generation poly(amidoamine) (PAMAM) dendrimers, terminated with amine groups (G6-NH_2), were purchased from Dendritech, Inc. (Midland, MI) as a 9.0 wt % solution in methanol. Prior to use, the methanol was removed under vacuum, and then the dendrimers were reconstituted in water to yield a 100 μM stock solution. A 0.50 M NaOH solution, $NaBH_4$ (99.9%), $HAuCl_4$ (≥99.9%), and HPLC grade 2-propanol (99.9%) were purchased from Sigma-Aldrich. K_2PtCl_4 (99.9%), $CuSO_4$ (98%, anhydrous), and NaCl were obtained from Fisher (NJ). A 70% $HClO_4$ solution (in H_2O) was purchased from Acros Organics (NJ).

Deionized (DI) Milli-Q water (18.2 MΩ cm; Millipore, Bedford, MA) was used for all solutions. Carbon- and lacey-carbon-coated Cu TEM grids were purchased from EM Sciences (Gibbstown, NJ, catalog numbers CF400-Cu-UL and LC400-Cu). Vulcan carbon (EC-72R) was obtained from ElectroChem, Inc. (Woburn, MA). PTFE membrane filters (0.5 μm pore size) were from Advantec MFS, Inc. (Dublin, CA). All electrodes were purchased from CH Instruments (Austin, TX) with the exception of the working electrode used to prepare the EXAFS sample, which was Toray Teflon-treated carbon paper (TGP-H-120) from The Fuel Cell Store (Boulder, CO).

Synthesis of Au Dendrimer-Encapsulated Nanoparticles (DENs). DENs are NPs synthesized using dendrimer templates, and they are characterized by a high degree of monodispersity in size, composition, and structure.[3,22,23] For this study, Au DENs were synthesized according to a literature procedure[45] with slight adjustments. Briefly, 147 equiv of $HAuCl_4$ (20 mM; 147 μL) was added dropwise to an aqueous G6-NH_2 solution with vigorous stirring. This results in encapsulation of $AuCl_4^-$ within the dendrimer. Reduction of this composite was achieved by adding an 11−12-fold excess of $NaBH_4$, contained in 0.3 M NaOH (1.0 mL), within <2 min. For this step, the NaOH was added to a weigh boat containing the $NaBH_4$ just before the mixture was transferred to the reaction solution. A color change from light yellow to brown signaled successful formation of Au_{147} DENs. Note that the Au_{147} DENs notation is not intended to imply that all DENs contain exactly 147 atoms, but rather the initial $AuCl_4^-$:G6-NH_2 stoichiometry. Following reduction, excess BH_4^- was deactivated by exposing the solution to air >12 h. No further purification was necessary. The final solution volume was 10 mL, and the concentration, with respect to the dendrimer, was 2.0 μM.

The DENs synthesis was slightly modified for EXAFS sample preparation. A total of 10 mL of 10 μM DENs was synthesized in two separate 5 mL batches, which each contained 500 μL of 100 μM G6-NH_2, 367.5 μL of 20 mM $HAuCl_4$, and ∼2.8 mg of $NaBH_4$ (a 10-fold excess) in 500 μL of 0.3 M NaOH. After ∼2.5 min of stirring, $NaBH_4$ and NaOH were added together to the solution as previously described. After deactivation of excess BH_4^- in air for >12 h, these DENs were dialyzed against 4.0 L of Milli-Q water for >12 h using 12 kDa MWCO dialysis tubing (Sigma-Aldrich).

NP Characterization. UV−vis spectroscopy was performed using a Hewlett-Packard 8453 spectrometer. Transmission electron microscopy (TEM) and scanning TEM (STEM) were performed using a JEOL 2010F TEM, having a point-to-point resolution of 0.19 nm and an operating voltage of 200 kV. Au_{147} DEN samples for TEM analysis were prepared by dropcasting 2.0 μL of the DEN solution onto a carbon-coated Cu TEM grid and then drying in air. STEM was used to image composite inks (described in the next section) consisting of Au_{147} DENs and Vulcan carbon (VC). These TEM samples were prepared by diluting the DEN/VC ink 1:6 with water, sonicating for ∼10 min, and then dropcasting (0.5 μL) onto a lacey-carbon-coated Cu grid. For AuPt DENs, lacey-carbon-coated Cu TEM grids were prepared by lightly swiping the electrode surface across the grid.

Electrochemical Synthesis of AuPt DENs via the HT Method. Electrochemical measurements were performed using a CH Instruments 627E potentiostat. For all experiments, an Hg/Hg_2SO_4 reference electrode and a glassy carbon rod counter electrode were used. Prior to use, the glassy carbon working electrodes (GCEs, 3 mm) were polished sequentially with 1.0, 0.3, and 0.05 μm alumina (2 min/pad) and then sonicated in water for ∼10 min to remove excess alumina. The DENs were dispersed onto VC as follows. The VC (∼1 mg) was first sonicated with 200 μL of isopropyl alcohol for ∼10 min to facilitate dispersion, and then 1.0 mL of 2.0 μM DENs was added. The resulting ink was sonicated for an additional 10−15 min. The DENs were immobilized onto the GCE by dropcasting 6.0 μL of ink

DOI: 10.1021/jacs.7b12306
J. Am. Chem. Soc. 2018, 140, 6249−6259

Table 1. Structural Parameters Extracted from Fitting the Au−L_3 and Pt−L_3 Edge Experimental (AuPt DENs) EXAFS Data and DFT Simulated EXAFS Data[a]

	N_{Au-M}	N_{Pt-M}	R_{Au-M} (Å)	R_{Pt-M} (Å)	ΔR (Å)	σ^2_{Au-M} (Å^2)	σ^2_{Pt-M} (Å^2)
Expt.	9.1(9)	10(2)	2.838(6)	2.77(2)	0.07(2)	0.0094(9)	0.008(5)
NP561 alloy	10.4	9.2	2.844	2.791	0.053	0.0128	0.0133
NP561 shell-1	10.2	9.6	2.834	2.805	0.029	0.0108	0.0117
NP453 shell-2	11.1	6.7	2.862	2.729	0.133	0.0206	0.0156
NP453 Pt cluster	10.6	7.7	2.869	2.742	0.127	0.0181	0.0213
Pt_{38}		7.6		2.697			0.0236

[a]N is coordination number (CN), R is bond length, ΔR is the difference between R(Au−M) and R(Pt−M), and σ^2 is the Debye−Waller factor.

and drying under a gentle N_2 flow. Electrochemical cleaning of the DENs was carried out by cycling the electrode potential 20 times from 0 to 0.80 to −0.70 V at 200 mV/s in 10 mL of N_2-purged, 0.1 M $HClO_4$.

The HT Pt deposition was performed in a 10 mL pH 4.0 solution containing 0.5 M NaCl and 3.0 mM K_2PtCl_4. The potential was first held at −0.014 V for 30 s (step 1 in Scheme 1) to clean the surface. Next (step 2), the potential was pulsed to −1.2 V for 1 s to deposit Pt and H_{ads}. Finally (step 3, red line), the potential was pulsed back to −0.014 V for 1 s to strip off the H_{ads} layer. At this point, the electrode was disconnected from the potentiostat (e.g., moved to the open circuit potential). To ensure that excess Pt^{2+} was removed from the electrode surface after HT deposition, the GCE was rinsed with DI water (~20 s), and then with 20 mL of 0.1 M $HClO_4$ (5 min, with stirring). Cyclic voltammograms (CVs) of the electrodes were subsequently recorded by scanning from 0 to 0.80 to −0.70 V at 100 mV/s in 10 mL of N_2-purged 0.1 M $HClO_4$. A total of six cycles were required to achieve consistent CV behavior. Electrochemical preparation of the EXAFS sample varied slightly and is discussed in section S1 in the Supporting Information.

Energy Dispersive Spectroscopy (EDS). EDS was performed using a Themis Z equipped with a monochromator, probe aberration corrector, and Super-X EDS technology. High-resolution, high-angle annular dark-field (HAADF) STEM was also performed using a DCOR+ probe aberration corrector and OptiSTEM+ aberration correction. A 70 μm aperture was used with a camera length of 115 nm and an accelerating voltage of 300 kV. The electron beam current for EDS was 350 pA, and the probe size was less than 0.1 nm. The total collection time was 6 min, and the dwell time was 23 μs. The EDS maps were acquired using a Thermo Scientific Themis Z microscope equipped with a Thermo Scientific Super-X detector system, which combines four symmetrically placed Si drift detectors around the objective lens with a high-brightness gun. This combination provides enhanced generation of X-rays and together with high detector efficiency results in a faster mapping of larger areas in EDS maps. Because of scheduling constraints, six months passed between preparation of the samples and analysis by the Themis. EDS for the EXAFS sample was performed using a JEOL 2010F TEM operated in STEM mode. One week passed between sample preparation and analysis of these materials.

Extended X-ray Absorption Fine Structure (EXAFS). The Au−L_3 and Pt−L_3 edge X-ray absorption fine structure (XAFS) measurements were performed in transmission and fluorescence modes at the BL2-2 beamline of the Stanford Synchrotron Radiation Lightsource (SSRL) at the SLAC National Accelerator Laboratory. Two 15 cm-long ionization detectors were used for measuring incident (with a 75:25 mixture of N_2 and Ar) and transmitted (with a 50:50 mixture of Ar and Kr) beam intensities. A third 15 cm ionization chamber (filled with a 50:50 mixture of Ar and Kr), located downstream of the transmission detector, was used to detect the beam through an Au foil reference for X-ray energy calibration and spectral alignment. The 13 channel Ge detector was used to measure fluorescence data that were used for Pt edge analysis. Both the Pt and the Au regions were measured in the same scan.

Computational Methods. Theoretical calculations were performed using the density functional theory (DFT) implemented in the Vienna ab initio simulation package (VASP).[46,47] Core electrons were described with the projector augmented-wave (PAW) method.[48,49] The Kohn−Sham wave functions for the valence electrons were expanded in a plane-wave basis set with an energy cutoff of 300 eV. The exchange-correlation energy was treated within the framework of the generalized gradient approximation. Specifically, PBEsol[50] was used, which is a modified form of the Perdew−Burke−Ernzerhof (PBE) functional designed to improve lattice parameters and surface energies in solids. A single Γ-point was sufficient for integration of the reciprocal space due to the finite nature of the NPs.

To simulate the EXAFS spectra, an ensemble of equilibrium structures at finite temperatures is required. To avoid the expensive molecular dynamics simulations using DFT, we employed an alternative methodology to sample the equilibrium structures by using DFT-evaluated dynamical matrixes. Dynamical matrixes for the systems of interest were obtained using a finite difference method in which a displacement of 0.01 Å was applied to every degree of freedom of the equilibrium structure. A set of $3N - 6$ harmonic oscillators with their force constants and vibrational normal modes were obtained by diagonalizing the obtained dynamical matrix. Statistically independent structures at finite temperatures were then sampled by displacing the atoms in the system along each normal mode with a magnitude following a Gaussian distribution. The standard deviation of the Gaussian distribution is described by eq 1, obtained using an approximation of a quantum harmonic oscillator. In this equation, M is the effective mass of the harmonic oscillator, ω is the vibrational frequency, $\hbar$ is Planck's constant, k_B is Boltzmann's constant, and T is the temperature.

$$\sigma = \sqrt{\frac{\hbar}{2M\omega}\coth\left(\frac{\hbar\omega}{2k_BT}\right)} \quad (1)$$

On the basis of the sampled structures, theoretical EXAFS spectra were simulated using an approach similar to that reported previously.[45,51] The Au− and Pt−L_3 edge EXAFS spectra were calculated from 300 structures by averaging the signal arising from each Au or Pt atom in the system. The multiple scattering calculations were performed using FEFF6-lite.[52] All atoms up to 6.0 Å away from each X-ray-absorbing atom were included in the scattering calculations. The experimental corrections to the photoelectron energy origin and the passive electron reduction factor were then applied to the simulated EXAFS spectra to align experimental and theoretical data in k-space and in amplitude, respectively.

The structural information presented in Table 1, including coordination numbers (CNs; individual values denoted as N), average nearest neighbor bond lengths (R), and the Debye−Waller factors (σ^2, defined as the variance of the metal−metal pair), as calculated by averaging the structural data of the 300 sampled equilibrium structures for each examined system. To calculate these values, a window of 2.5−3.3 Å was used to define the first nearest neighbors in r-space.

Au surface segregation energies were calculated as the total energy difference between the segregated and the nonsegregated models: $dE_{seg} = E_{seg} - E_{no\_seg}$. Ab initio molecular dynamics simulations were employed to equilibrate the structures of Pt-decorated Au nanoparticles. A time step of 1.5 fs was used, and 5000 total steps (7.5 ps) were carried out for each MD simulation. The temperature was held at 300 K by rescaling the velocities of all atoms every 10 steps.

DOI: 10.1021/jacs.7b12306
J. Am. Chem. Soc. 2018, 140, 6249−6259

RESULTS AND DISCUSSION

Synthesis and Characterization of Au_{147} DEN Cores. Details of the synthesis of the Au_{147} DENs are described in the Experimental Section. Briefly, 147 equiv of $HAuCl_4$ was mixed with G6-NH_2 dendrimers, and then the mixture was reduced using excess $NaBH_4$. As we have discussed previously, this process results in nearly size monodisperse Au DENs.[3]

A UV−vis spectrum of the Au_{147} DENs solution is shown in Figure S1a. It reveals a monotonic increase in absorbance in the direction of higher energy that is characteristic of NP formation.[53] A small AuNP plasmon band at ∼520 nm indicates that the NP size is <2 nm.[36] STEM analysis (Figure S1) confirms that: the Au_{147} DENs are 1.6 ± 0.3 nm in diameter, which is in good agreement with previous reports[34,35,36,45,51] and the predicted size for a 147-atom cuboctahedral Au particle (∼1.6 nm).[36]

Synthesis and Characterization of AuPt DENs. The HT method used to deposit Pt on the Au_{147} DENs is described in detail in the Experimental Section. Briefly, a conductive ink containing ∼1 mg VC/mL and 2.0 μM Au_{147} DENs was dropcast (6.0 μL) onto a polished GCE, dried under a gentle flow of N_2, and then cleaned electrochemically. Figure 1a (black trace) is a CV of the resulting Au_{147} DEN-modified GCE. The positive scan limit (0.80 V) was chosen such that qualitative changes in the Au electrochemically active surface area could be determined, but without changing the structure of the Au_{147} DENs. Au oxide formation is apparent positive of ∼0.50 V, and the corresponding oxide reduction peak is centered at ∼0.41 V. These values are in agreement with our previous reports for Au_{147} DENs.[34,35,36]

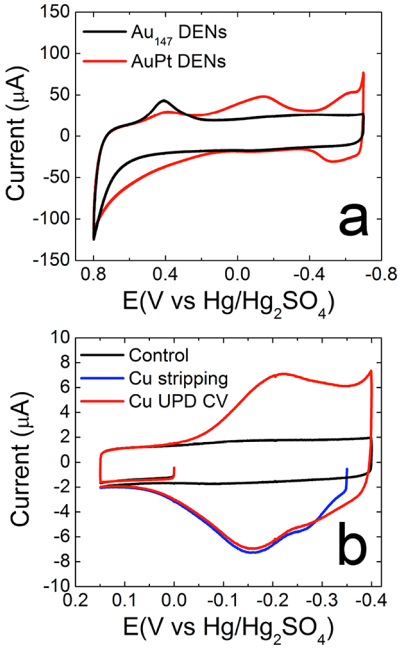

Figure 1. (a) Cyclic voltammograms (CVs) before (black) and after (red) HT Pt deposition on Au_{147} DENs. The electrolyte solution was N_2-purged, 0.1 M $HClO_4$, and the scan rate was 100 mV/s. (b) CVs corresponding to Cu UPD on AuPt DENs. A Cu UPD CV is shown in red, and a background CV (no Cu^{2+}) is provided for comparison (black). The blue LSV was recorded after Cu^{2+} electrodeposition for 300 s at −0.35 V. The scan rate was 10 mV/s, the electrolyte solution was N_2-purged, 0.1 M $HClO_4$ containing 5.0 mM $CuSO_4$. For both (a) and (b), the DENs were immobilized onto the GCE working electrode using a VC ink.

Following electrochemical characterization of Au_{147}, Pt was deposited following the procedure summarized by Scheme 1 and described in the Experimental Section. This method is very similar to that used by Moffat and co-workers,[7] with the exception that in our case the duration of step 3 was just 1.0 s rather than 30.0 s (Scheme 1, red line). Following Pt deposition, the GCE was rinsed briefly in DI water and then in 0.1 M $HClO_4$ for 5 min to remove any excess Pt^{2+} that might be present. The red trace in Figure 1a is a CV of the resulting material, recorded immediately after the acid rinse. It reveals Pt hydride waves between −0.40 and −0.67 V, a broad feature associated with Pt oxidation positive of ∼0.15 V, and a Pt oxide reduction peak centered at ∼ −0.14 V. An Au oxide reduction peak centered at ∼0.40 V is also present.

Comparing the black and red CVs in Figure 1a, the most notable changes after Pt deposition are the appearance of Pt-specific peaks (hydride and oxide) and attenuation of the Au oxide reduction peak. These features indicate, at least qualitatively, that some Pt is present on the surface of the Au_{147} DENs. Specifically, the potentials for the Pt hydride adsorption/desorption peaks are in good agreement with those previously reported for Au@Pt DENs[35] and Pt DENs.[37] Importantly, however, the presence of the attenuated Au oxide reduction peak suggests that both Au and Pt are present on the NP surface.

We carried out several important control experiments to provide confidence in the results described thus far. For example, Figure S2 shows that when the HT method is applied to Au_{147} DENs, the amount of Pt deposited is independent of pulse time within the range of 1−10 s, thus confirming that deposition is self-limited during the 1 s pulse used in our experiments. Even pulses of 100 s lead to only a slight increase in Pt deposition. Another control experiment is discussed at length in section S2. Here, electrochemical and microscopy data indicate that negligible amounts of Pt-only NPs form in the absence of the Au_{147} DEN cores. In other words, nearly all of the Pt on the GCE is deposited on the surface of the Au_{147} DEN cores.

Scanning Transmission Electron Microscopy (STEM). Figure 2 displays a STEM micrograph and a size-distribution histogram for AuPt DENs synthesized using the HT method. The AuPt DENs are 2.8 ± 0.6 nm in diameter, which can be compared to the original size of the Au_{147} DEN cores (1.6 ± 0.3 nm) and the calculated size of a 147-atom cuboctahedral AuNP capped with a single ML of Pt (∼2.1 nm).[36] Note that

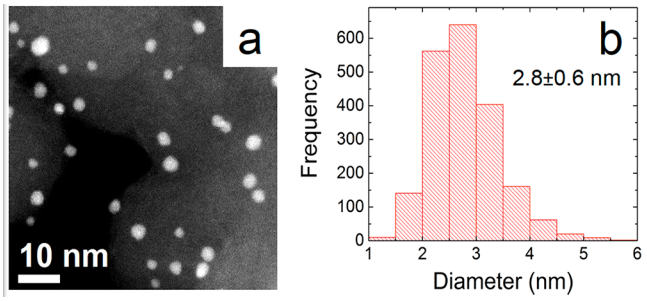

Figure 2. (a) STEM micrograph for the AuPt DENs. (b) A size-distribution histogram obtained using numerous micrographs like that shown in (a).

DOI: 10.1021/jacs.7b12306
J. Am. Chem. Soc. 2018, 140, 6249−6259

we have previously reported sizes of 2.3 ± 0.4 nm for Au_{147}@Pt DENs prepared by UPD of Pb followed by Pt GE,[36] and 2.5 ± 0.4 nm for Au_{140}@Pt DENs prepared by Cu UPD followed by Pt GE.[38] Therefore, the average NP size achieved using the HT method is, within error, consistent with results obtained for these closely related materials.

Energy Dispersive Spectroscopy (EDS). EDS mapping (Figure 3) was used to confirm selective deposition of Pt on the AuNPs. The key result is that Au and Pt are colocalized on the same NPs. Apart from this qualitative statement, there is insufficient resolution in the EDS data to draw quantitative conclusions about structure (i.e., the relative locations of Au and Pt). For structural information, therefore, we relied upon electrochemical methods, X-ray absorption spectroscopy (XAS), and theoretical calculations (vide infra).

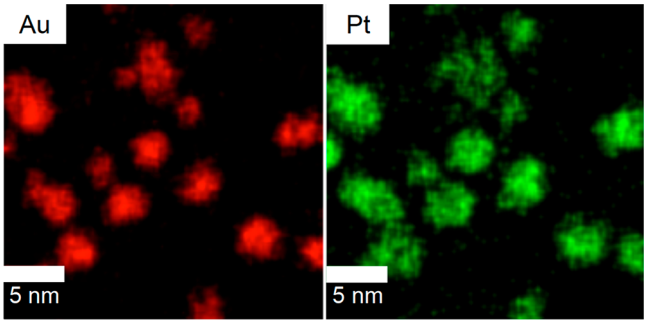

Figure 3. Au and Pt EDS maps for AuPt DENs.

Although the Pt EDS signals are primarily concentrated in regions where the NPs are located, we also note that there is a low level of stray Pt signals elsewhere. This is likely noise. Indeed, as mentioned previously, a series of control experiments (section S2) showed that HT Pt deposition is selective for the NPs.

Surface Composition. As discussed in the context of Figure 1a, hydride adsorption occurs on Pt but not Au, and therefore it can be used to estimate the surface area of Pt. Cu UPD, on the other hand, occurs on both Au and Pt,[40] and therefore it provides information about the total NP surface area. By comparing the Pt and total surface areas, the percentage of Pt on the surface of the NPs can be deduced.

Cu UPD was performed on freshly prepared AuPt DENs immediately following determination of the Pt surface area. The first step was to obtain a background CV of the AuPt DEN-modified electrode in the absence of Cu^{2+} (black trace, Figure 1b). This CV was obtained by holding the potential of the electrode at 0 V for 300 s, and then scanning it between 0.15 and −0.40 V. Only capacitive current is observed.

The Cu UPD CV (red trace) was obtained by adding 100 μL of 0.50 M $CuSO_4$ to the 10 mL solution used for the black trace and scanning the electrode over the same potential range. Cu UPD occurs at nearly the same potential on Au[54] and Pt[37,43,54,55] DENs, so only a single peak is observed, and it is centered at −0.22 V. Upon scan reversal, two Cu oxidation peaks are centered at −0.27 and −0.16 V. These values are consistent with a previous report for Au_{140}@Pt DENs.[38,54] This experiment provides the information necessary about potential scan limits to calculate surface areas.

To obtain the total NP surface area, the following experiment was carried out. First, a ML of Cu was deposited by holding the electrode potential at −0.35 V for 300 s. Second, the ML was stripped off by scanning from −0.35 to 0.15 V. Finally, the Cu stripping voltammogram (blue trace) was baseline subtracted (black trace), and the resulting area under the curve was integrated to obtain the total charge corresponding to Cu UPD.

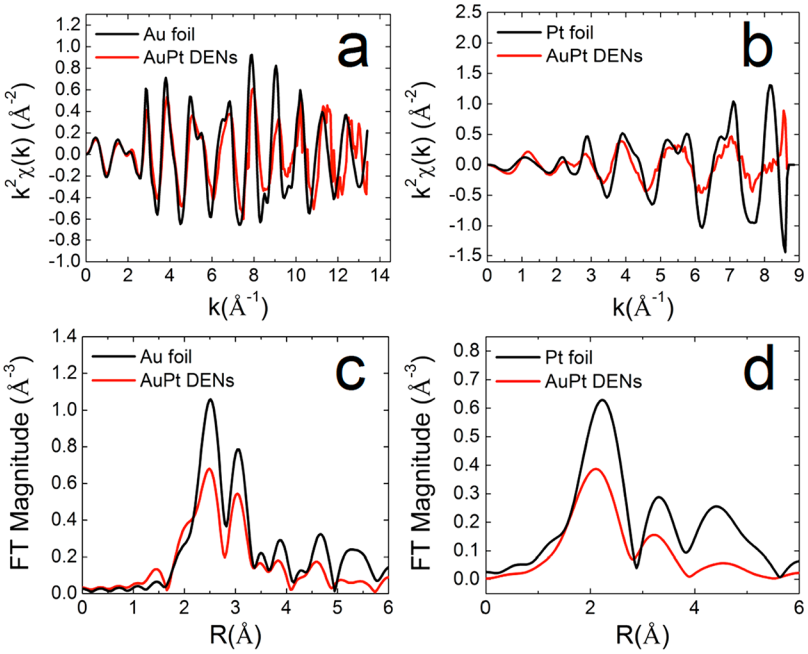

Figure 4. (a,b) Comparison of the *k*-space Au−L_3 and Pt−L_3 edge EXAFS spectra for AuPt DENs and Au and Pt reference foils. (c,d) Fourier transform (*r*-space) Au−L_3 and Pt−L_3 edge EXAFS spectra for AuPt DENs as compared to Au and Pt reference foils. The *k*-space and *r*-space ranges used for the fitting were 2.66−7.00 $Å^{-1}$ and 1.50−3.77 Å, respectively, for Pt and 2.00−11.00 $Å^{-1}$ and 2.19−3.28 Å, respectively, for Au. These spectra were used to determine the average coordination numbers (CNs), Au−M and Pt−M bond lengths, and the Debye−Waller factors (Table 1).

DOI: 10.1021/jacs.7b12306
J. Am. Chem. Soc. 2018, 140, 6249−6259

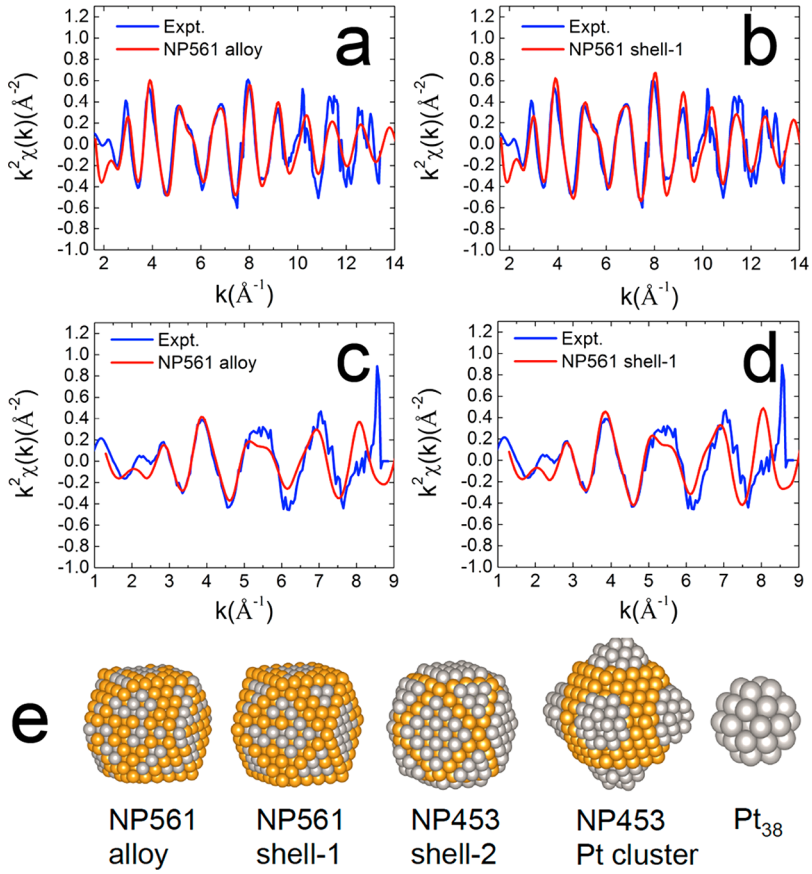

Figure 5. Comparisons between DFT simulated (red) and experimentally obtained (blue) (a,b) Au-L_3 and (c,d) Pt-L_3 edge spectra, plotted in *k*-space for the (a,c) NP561 alloy and (b,d) NP561 shell-1 models. (e) Visual depictions of the models considered: random or quasi-random alloy (NP561 alloy), core@partial Pt shell with Au surface segregated to occupy the corner and edge atoms of the NP shell and 45 Pt atoms located subsurface (NP561 shell-1), two-dimensional Pt patch model (NP453 shell-2) where corner and edge atoms were removed to shrink the size of the Pt patches and shorten R(Pt−M), three-dimensional Pt cluster model (NP453 Pt cluster) with an Au core and segregated three-dimensional Pt patches, and Pt_{38}, which tests the possibility of small Pt clusters in the sample. Simulated spectra for the latter three structures are located in Figure S8. Cuboctahedral geometry was used for all models.

The charge densities for Cu UPD on bulk Au[34] and Pt[56] are roughly equivalent (405 and 410 $\mu C/cm^2$), and therefore we used the averaged value of 407.5 $\mu C/cm^2$ to determine the total NP surface area. The amount of Pt on the surface was determined by integrating the hydride waves (Figure 1a, red CV) and using the value of 210 $\mu C/cm^2$ to convert charge to surface area.[34] Using these values, and the experimentally determined charges associated with Cu UPD (103 μC) and Pt hydride (27.5 μC), we calculated total and Pt-only surface areas of 0.25 and 0.13 cm^2, respectively. The key finding, then, is that on average ∼52% of the NP surface is Pt and ∼48% is Au. If the HT method resulted in Pt depositing exclusively on the NP surface, we would not expect to observe any surface Au. The fact that Au and Pt are both present in approximately equal measure on the NP surface suggests these materials have a more complex structure than a simple Au@Pt core@shell configuration.

EXAFS. Substantially more DENs are necessary for EXAFS measurements than for the electrochemical experiments described thus far, and therefore slight adjustments to the synthetic method were required. These, along with TEM characterization data, are discussed in section S1. Electrochemical features of the NPs prepared for EXAFS are in good agreement with the non-EXAFS samples, although the CVs (Figure S3) indicate slightly more Au on the surface of the EXAFS NPs. Cu UPD data for the EXAFS sample, discussed in section S3, indicate a surface composition of 42 ± 2% Pt, which is comparable to the non-EXAFS sample (52 ± 5%). EDS for the EXAFS sample (Figure S4) shows that Au and Pt are colocalized within the NPs, just as they were for the non-EXAFS sample.

Analysis of the experimental EXAFS (Figure 4) was performed to further refine the AuPt NP structure. This analysis is complicated by the fact that Au and Pt have overlapping L_3-edge spectra.[57,58] As a result, it was only possible to extract the total Au and total Pt CNs: *N*(Au−M) and *N*(Pt−M). For the general case, we define *N*(A−M) as equal to the sum of *N*(A−A) and *N*(A−B) for elements A and B.[57] Because of the low amount of sample (∼9−10 mg VC/DENs with a weight loading of 32% metal, in an ∼0.36 cm^2 area), and thus the expected poor signal-to-noise ratio in the Pt−L_3 EXAFS spectrum past the Au−L_3 edge, we analyzed the Pt- and Au-edge data separately and did not employ the general analysis scheme for bimetallic compositions with overlapping edges.[57,58] Additional fitting considerations are discussed in section S4. Table 1 shows the Au−M and Pt−M CNs, bond lengths, and the associated Debye−Waller factors. We interpret these parameters in a later section.

Figure 4 shows the edge-step normalized, background-subtracted data in *k*- and *r*-space for the Au−L_3 and Pt−L_3

DOI: 10.1021/jacs.7b12306
J. Am. Chem. Soc. 2018, 140, 6249−6259

edges. Fourier transform magnitudes of the data and best fits are shown in Figure S5a–d for the Au and Pt edges. The Au–L_3 edge XANES spectrum for the AuPt DENs is almost identical to that of the Au foil (Figure S6a), indicating that the Au atoms in the NPs are in the metallic state (zerovalent). The particle size effect is evidenced by reduction of the oscillation intensity in *k*-space and Fourier transform intensities in *r*-space in the NP spectra as compared to their bulk foil counterparts (Figure 4a and c). We note that from the similarity of the spectra to that of the Au foil alone, one cannot make a conclusion that the Au phase in the NPs is mixed with Pt or segregated. Au and Pt atoms do not have sufficient *Z*-contrast to make such a determination from just the visual observation of Au–L_3 edge spectra. Such analysis will be done using a theoretical fitting approach described in the next section.

As is evident in Figure S6b, the AuPt DENs Pt–L_3 edge is shifted toward higher energy, and has higher intensity in the whiteline region, as compared to the reference Pt foil. These observations indicate that the electronic density is distributed differently around Pt atoms in the NPs as compared to bulk Pt. This observation would have been consistent with oxidation, but Figure S5c,d shows that the Pt–M contribution provides an adequate fit (*R*-factor = 0.017) to the experimental spectra without the addition of any Pt–O contribution. This behavior is thus likely due to the alloying of Pt and Au in the NP. Jose-Yacaman and co-workers showed that for Au@Pt core@shell NPs the Pt edge XANES data were not significantly shifted relative to both PtNPs and a Pt foil, indicating segregation.[59] We will revisit this possibility below, when we interpret the results of quantitative analysis of EXAFS spectra by theoretical fitting.

The best fit values of the adjustable parameters for all of the samples and their reference foils are reported in the first row of Table 1. Table 1 shows that the CNs of the Au–M (9.1 ± 0.9) and Pt–M (10 ± 2) contributions are the same, within the uncertainties. These CN values favor a model in which the Au and Pt atoms are distributed randomly, or quasi-randomly, within the NPs. Only in that case would the Au–M and Pt–M CNs be approximately equal, due to an Au atom having the same probability as a Pt atom to be located on the surface or interior of the NP. The proposed alloy structure is also consistent with the strongly altered shape of the Pt–L_3 edge XANES (vide supra) as compared to the monometallic Pt foil. Interpretation of the extracted bond lengths is not immediately straightforward for predicting component distribution because, in addition to the bond length dependence on the degree of mixing, it also depends on the NP size.

In summary, on the basis of the CNs of Au–M and Pt–M contributions and the modified electronic structure apparent in the Pt–L_3 edge XANES data, we propose that the structure of the AuPt DENs is an alloy. As we will discuss in the Theoretical Modeling section, next, the alloying is likely localized primarily in the NP shell, and therefore the structure is more likely a quasi-random alloy rather than a true random alloy.

The Au:Pt edge-step ratio measured by XANES (Figure S6) was used to determine the total NP composition for the EXAFS sample. XANES, rather than XPS, was used for this purpose because of the greater penetration depth afforded by X-ray absorption spectroscopy. The edge-step ratio, analyzed with XAFSmass,[60] indicates that the sample is 73% Au and 27% Pt.

Theoretical Modeling. Figure S7 demonstrates the predictive power of DFT for EXAFS signals, tested by comparing experimental and DFT-simulated Au and Pt foil *k*-space spectra. As shown, reasonable fits were obtained in terms of both amplitude and phase shift, with slightly better modeling of the Au edge relative to the Pt edge. Figures 5 and S8 compare the theoretical EXAFS signals generated with various atomic models with experimental measurements. First, we examined two models with cuboctahedral geometry for 561 total atoms (with 252 surface atoms) and total NP composition ($Au_{410}Pt_{151}$) determined from the XANES data. Assuming strictly two-dimensional growth, 106 Pt atoms (42% coverage according to the Cu UPD data) are randomly distributed or clustered on the surface, which are labeled as NP561 alloy and NP561 shell-1, respectively. Subtracting surface Pt composition from total Pt composition, 45 other Pt atoms are randomly distributed in the core of the NPs (overall $Au_{264}Pt_{45}$@ $Au_{146}Pt_{106}$).

For the core@partial shell structure (NP561 shell-1), theoretical modeling shows that the most favorable arrangement is one in which the Au atoms surface segregate to occupy the corner and edge sites first. Given the short *R*(Pt–M) from experiment, three other models with a higher degree of Au and Pt segregation were tested: a two-dimensional Pt patch model (NP453 shell-2), which places all of the Pt atoms in the sample on the NP surface and removes the corner and edge atoms to shrink the Pt patches (effectively shortening *R*(Pt–M)); a three-dimensional Pt shell model (NP453 Pt cluster) having an Au core and a shell composed of three-dimensional Pt patches; and a Pt_{38} monometallic NP to test the possibility of individual Pt clusters being present in the sample. Simulated spectra for the latter three structures are provided in Figure S8. The importance of including vibrational disorder in the atomic models is illustrated in Figure S9.

Table 1 compares the experimental and simulated EXAFS parameters. As shown, the NP561 alloy and NP561 shell-1 structures fit the experimental data most closely in terms of the predicted CNs (*N*), bond lengths (*R*), difference between the bond lengths (ΔR), and the Debye–Waller factors (σ^2). The shell-1 model shows a slightly better prediction of *N*(Pt–M) than the alloy model, although both models are within error of the experimental *N*(Pt–M). *N*(Au–M) for the shell-1 model is slightly closer (10.2) to the experimental value than is the alloy model (10.4). However, both models slightly overestimate the experimental *N*(Au–M) (8.2–10.0). This may be explained by the somewhat heterogeneous size distribution of the EXAFS sample. We discuss the bond length trends later.

Table S1 provides the *R*-factors calculated for each model for the Au–L_3 and Pt–L_3 edges. These *R*-factors signify the relative difference between the simulated and experimental spectra; lower values denote better fits.[61] The alloy and shell-1 models exhibit the best fits to the experimental *k*-space spectra for both the Au–L_3 and the Pt–L_3 edges (Figure 5a–d and Figure S8). As shown in Figure 5a,b, the shell-1 model qualitatively fits the Au–L_3 edge experimental data slightly better at high *k*-values than does the alloy model. This is likely a result of slightly better modeling of disorder given that σ^2_{Au-M} is closer to the experimental value for the shell-1 model than for the alloy model. However, Table S1 indicates a smaller *R*-factor, and thus a better Au–L_3 edge fit, for the alloy model. The NP453 Pt cluster and NP453 shell-2 models (Figure S8a,b) qualitatively demonstrate significant inefficiency in modeling the Au–L_3 edge disorder at higher *k*-values, as shown by the poor alignment to the experimental peak amplitudes. The shell-2 model was better than the NP453 Pt cluster model in this regard, and the *R*-factor for the shell-2 model is identical to that

DOI: 10.1021/jacs.7b12306
J. Am. Chem. Soc. 2018, 140, 6249–6259

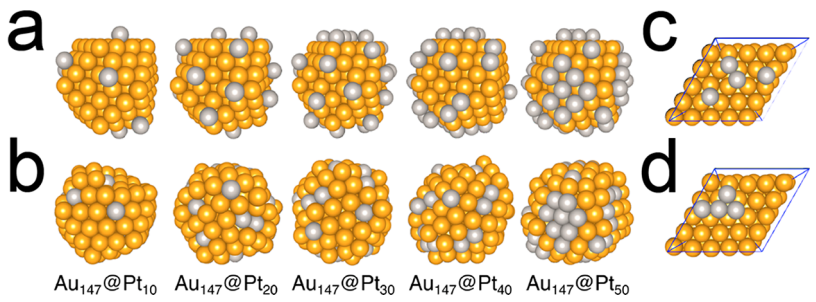

Figure 6. Ab initio molecular dynamics simulations for Pt deposited on (a,b) Au_{147} NPs and (c,d) Au(111). Pt initially adsorbs to each surface (a,c). After 7.5 ps equilibration at 300 K, Pt embeds into the NP surface (b), but not into Au(111) (d). Pt incorporation into the NPs is observed over a range of Pt compositions (10−50 Pt atoms or 6−25%).

of the shell-1 model. The NP453 Pt cluster model demonstrates the greatest misfit (highest *R*-factor) of all of the models to the Au−L_3 edge.

For the Pt−L_3 edge spectra (Figure 5c,d, Figure S8c−e, and Table S1), none of the fits are ideal, possibly as a result of the limited *k*-range due to overlapping Au−L_3 and Pt−L_3 edges. Qualitatively, the alloy (Figure 5c) and shell-1 (Figure 5d) spectra demonstrate similar fits to the experimental spectra, with a slightly better match in amplitude for the shell-1 model due to a higher CN. The *R*-factors for the Pt−L_3 edge reveal similar misfits for the alloy and shell-1 models, with a better match for the alloy model. The NP453 Pt cluster (Figure S8c) and NP453 shell-2 (Figure S8d) models have worse qualitative fits than either the alloy or the shell-1 model at higher *k*-values. Indeed, the *R*-factors for the Pt-L_3 edge fits are significantly higher for the NP453 Pt cluster and shell-2 models than for the shell-1 model. The Pt_{38} model shows both the worst qualitative (Figure S8e) and quantitative (*R*-factor = 1.21) agreement with the experimental data by far and suggests that if any small Pt clusters are present, they are not the predominant form of Pt (recall that EXAFS is an ensemble technique).

Despite the slightly better agreement between predicted and experimental EXAFS parameters (Table 1) for the shell-1 model relative to the alloy model, the alloy model is more likely based on three features: (1) *R*-factors, (2) the values of ΔR (Table 1), and (3) the XANES data. As shown in Table S1, the *R*-factors are smallest for the alloy model, for both the Au−L_3 and the Pt−L_3 edges. Thus, the alloy model has a better overall fit than does the shell-1 model.

Because the bond lengths are affected by both size effects and composition, the difference, ΔR, between *R*(Au−M) and *R*(Pt−M) is more important than the exact, predicted values. The value of ΔR predicted by the alloy model (0.053 Å) fits the experimental value (0.07 Å) within the error of the experimental measurement (±0.02 Å), whereas ΔR for the shell-1 model (0.029 Å) does not. Although the three-dimensional cluster model (NP453 Pt cluster) predicts CNs close to being within error of the experimental data, ΔR for that model is nearly double (0.127 Å) the experimental ΔR. Therefore, although the amount of segregation may be greater than predicted by the ideal alloy structure, it is much less than predicted by the NP453 cluster model. One possible explanation for why the experimental ΔR is on the high end of the predicted alloy value is heterogeneity in bond lengths as a result of heterogeneity in the NP size-distribution (3.2 ± 0.7 nm). However, as previously mentioned, ΔR for the alloy model is still within error of the experimental value.

As discussed in the EXAFS section, the XANES data (Figure S6b) show electronic modification of the Pt−L_3 edge that suggests alloying. The XANES data in combination with the experimental/theoretical agreement for the *R*-factors and for ΔR indicate that the alloy structure is more likely than the shell-1 model, perhaps with a small degree of segregation. However, we believe the structure is quasi-random rather than completely random due to the higher concentration of Pt in the shell than in the core.

Mechanism of Alloy Formation. As we will discuss in the next section, the summation of all of our data indicates that the alloy structure is the most likely. This is not entirely surprising. While Au and Pt are immiscible,[62] there is a tendency for Au and Pt to alloy at the nanoscale depending on the size of the NPs, the Au:Pt ratio, and the preparation method.[63] Additionally, despite classical immiscibility, there is precedent for significant bulk phase AuPt surface alloying as a result of kinetically limited Au surface segregation.[64,65] Importantly, however, our results compare structures of NP and bulk materials prepared using the same synthetic method. Scanning tunneling microscopy (STM) of the material resulting from HT Pt deposition on bulk Au(111) revealed ∼85% Pt coverage and limited AuPt surface alloying.[7] Significant surface alloying was later reported,[8] but only after intensive electrochemical cycling (70−200 cycles). Therefore, the extensive NP surface alloying (42−52% Pt) observed in the present study differs substantially from that of the corresponding bulk material.

While the exact details of alloy formation are unclear, we wish to propose a tentative mechanism (although we acknowledge that it is imperfect). Specifically, we evaluate two possible methods for alloying: Au surface segregation and Pt absorption. We posit that the latter is dominant.

AuPt mixing is usually ascribed to Au surface segregation arising from lower Au surface energy.[63,64] Our calculations (Figure S10) for Au surface segregation energy (E_{seg}^{Au}) confirm favorable Au surface segregation for Au(111) covered with a Pt ML (E_{seg}^{Au} = −0.26 eV), but show that it is suppressed when H is adsorbed to Pt (E_{seg}^{Au} = +0.23 eV).

The same trend is observed for a NP model. Specifically, we calculated E_{seg}^{Au} for a slightly smaller NP model (Au_{147}@Pt) than those shown in Figure 5e to reduce computational cost. We expected enhanced Au surface segregation for the NP system because of the higher curvature and the surface stress exerted on Pt by the Au−Pt lattice mismatch. This prediction is confirmed in Figure S11a−e, where we show that Au surface segregation is more favorable at the corner, edge, and (100) facets of the Au_{147}@Pt NP as compared to the Au(111)/Pt surface. However, Au surface segregation is suppressed at the

DOI: 10.1021/jacs.7b12306
J. Am. Chem. Soc. 2018, 140, 6249−6259

NP (111) facet. Once H is adsorbed to Pt on the NP surface (Figure S11f–j), Au surface segregation becomes energetically unfavorable for all sites. These results suggest that alloying via Au surface segregation would occur after H is stripped (step 3, Scheme 1) rather than during Pt deposition (step 2, Scheme 1).

The second and more probable mechanism is alloying during Pt deposition. The previous arguments were based on the assumption that the HT method produces an Au@Pt core@full shell structure in the first place. However, as we discuss in the next section, the total Pt composition in our sample (27%) is lower than that required to form a full Pt shell (45%). As we discuss later in this section, Au surface segregation becomes unfavorable when there are a large number of Au atoms already on the NP surface.

For the following discussion, we assumed that Pt atoms arrived at the AuNP surface one-by-one from all directions rather than spontaneously forming a full Pt shell. This differs from the UPD/GE technique, which uses a preformed (UPD) shell as a template for the Pt shell. We then carried out further calculations showing that alloying occurs rapidly during Pt deposition. Specifically, ab initio molecular dynamics (MD) simulations were performed to equilibrate the system at 300 K for 7.5 ps. The resulting structures show that the Pt adatoms and small Pt islands (Figure 6a) do not stay adsorbed to the outer AuNP surface; rather, they are absorbed by the AuNP and become embedded in the AuNP surface (Figure 6b) to increase their CNs. This effect is observed over a range of Pt compositions (6–25% or 10–50 atoms). A similar mechanism has been reported for Au absorption into Pd_6CoCu alloys.[66] The results before and after equilibration (Figure 6a,b) show that absorption occurs so quickly (7.5 ps) that a Pt shell cannot form on the NP surface. Figure S12 shows identical results for an icosahedral NP with 25% Pt (chosen to best match the experimental composition: 27% Pt), demonstrating that Pt incorporation is not due to the particular cuboctahedral shape selected.

In contrast to AuNPs, Pt adatoms on the bulk Au(111) surface form only Pt islands after 7.5 ps of equilibration (Figure 6c and d). On the basis of these results, we propose that AuPt NP alloying occurs at the Pt deposition stage due to the structural flexibility of the AuNPs. Pt adatoms are expected to remain adsorbed to the more rigid bulk Au(111) surface and simply form larger Pt islands, and eventually a Pt shell. Thus, our calculations bolster the assertion that different bulk and NP structures form upon application of HT Pt deposition on Au.

We contend that the second mechanism is more likely for three reasons. First, Pt incorporation is more rapid (7.5 ps) than the experimental Pt deposition time scale (1 s). Thus, Pt absorbs before the end of Pt deposition, during which time adsorbed H prevents competing Au surface segregation. Second, the Au surface segregation mechanism was formed on the basis of the assumption of full Pt shell formation. However, the Pt composition (27%) is less than required for a full Pt shell (45%).

Third, the AuPt alloy formed during Pt deposition has a lower driving force for Au surface segregation after the adsorbed H is stripped. To verify this assertion, we calculated E_{seg}^{Au} for MD equilibrated $Au_{147}@Pt_{50}$. These calculations (Figure S13) confirm that Au surface segregation is suppressed or even reversed when there is an incomplete Pt shell. We attribute this effect to the fact that for a Pt composition of 25%, there are already many Au atoms on the surface without the occurrence of Au surface segregation. This lowers the driving force for Au surface segregation. Hence, when the NP surface is not fully covered with Pt, Au surface segregation is not likely to be the dominant alloying mechanism.

Structure Determination. On the basis of results from Moffat and co-workers for HT deposition of Pt onto bulk Au,[7] we anticipated that AuPt DENs synthesized using the HT method would yield a simple core@shell structure. However, this was not the case. In this section, we provide a logical argument, based on results from TEM, EXAFS, XANES, electrochemistry, and theory, for the most consistent structure. We approach the problem using a process of elimination.

The least likely structure of the HT AuPt NPs is core@full shell. A 561-atom cuboctahedral Au@Pt NP has 252 surface atoms. In other words, this structure would contain 45% Pt if a full Pt shell were deposited. The Au:Pt ratio derived from XANES is 73:27 ($Au_{410}Pt_{151}$), indicating a total of 151 Pt atoms. Even if all of these were on the NP surface, they would not constitute a full 252-atom Pt ML. Electrochemical Cu UPD results indicate ~42% (106) Pt surface atoms, which is less than the total number of Pt atoms determined by XANES. Thus, comparison of the total and surface-only Pt composition suggests that either a small amount of Pt is incorporated into the NP core or that there is three-dimensional growth of Pt nodules onto the Au core. We will discuss each of these possibilities in due course.

The EXAFS CNs similarly fail to support a full Pt shell. For an ideal cuboctahedral core@shell Au@Pt NP, we would expect N(Au–M) to be ~12, given that each core Au atom would be fully surrounded by metal atoms, and that N(Pt–M) < N(Au–M), because NP surface atoms are under-coordinated.[67] In fact, however, the EXAFS data show that N(Au–M) ≈ N(Pt–M) within uncertainty. Therefore, XANES, Cu UPD, and EXAFS all disfavor a simple core@full shell model.

Next, we show that a core@partial-shell structure is less likely than an alloy structure. The two core@partial shell models analyzed (NP561 shell-1 and NP453 shell-2) display greater misfits to the experimental EXAFS spectra (higher R-factors) than does the alloy model. This is especially true for the NP453 shell-2 fit to the Pt–L_3 edge. The NP453 shell-2 model is easier to discard due to poor agreement with the experimental EXAFS parameters (Table 1) and the fact that the shell-2 NP surface consists of 83 exposed core Au atoms and 144 Pt shell atoms (63% surface Pt), which is higher than experimentally observed (42% surface Pt). Elimination of the shell-1 model is based on the fact that it was built assuming the Au surface segregation mechanism discussed in the previous section, with Au atoms placed at the corner and edge sites of the NP. However, we showed that for the HT synthesis, Au surface segregation is blocked due to H adsorption (Figure S11f–j) during Pt deposition. Rather, alloying via rapid Pt incorporation (7.5 ps) during Pt deposition is predicted (Figure 6), and Au surface segregation largely loses its driving force by the time the H is stripped (Figure S13). The higher R-factors for the NP561 shell-1 and NP453 shell-2 models, the poor EXAFS agreement and overestimated surface Pt content for the NP453 shell-2 model, along with the mechanism we propose for structure formation suggest that both core@partial-shell structures are unlikely.

We now consider the case of a random alloy structure. The first point in favor of a random alloy is that the values of N(Au–M), 9.1 ± 0.9, and N(Pt–M), 10 ± 2, extracted from EXAFS, are roughly equal within experimental error.[67] Although there is slightly better agreement between the

DOI: 10.1021/jacs.7b12306
J. Am. Chem. Soc. 2018, 140, 6249–6259

experimental and predicted EXAFS parameters for the core@partial-shell model (NP561 shell-1), the alloy model has the closest fit (lowest *R*-factor) to the *k*-space spectra for both the Au−L_3 and the Pt−L_3 edges and ΔR is within experimental error for the alloy model but not for the core@partial-shell model. Additionally, the XANES data suggest Pt alloying, as demonstrated by a Pt−L_3 edge shift to higher energy and the increase in whiteline intensity (coupled with a lack of evidence for Pt oxidation). Thus, EXAFS and XANES are consistent with a random alloy structure. Finally, MD simulations suggest that the random alloy structure is most likely from a kinetic point of view. However, the majority of the total Pt atoms (151) in the sample are on the surface (106). Accordingly, we believe these materials are quasi-random alloys.

Finally, we discuss the possibility of atomic arrangements incorporating three-dimensional Pt growth (NP453 Pt cluster and Pt_{38}, Figure 5e). The first arrangement that can be discounted is fully segregated Au and Pt NPs. The strongest evidence against this configuration is that EDS showed colocalization of Au and Pt for both the non-EXAFS (Figure 3) and the EXAFS (Figure S4) NPs. The CV data also argue against segregation. Specifically, upon HT electrodeposition, the Au electrochemically active surface area decreases while the electrochemical signature of Pt simultaneously increases. This indicates that Pt covers at least some of the Au on the NP surface. Moreover, the XANES spectrum indicates charge transfer between Au and Pt, suggesting that the two elements are in physical contact. Finally, models incorporating three-dimensional Pt growth exhibit significantly worse agreement with the experimental EXAFS data than the alloy model (Tables 1 and S1).

SUMMARY AND CONCLUSIONS

There are two major outcomes of the work reported here. First, we have shown that HT deposition of Pt onto 1.6 nm Au_{147} DENs yields a quasi-random alloy structure. This result is in contrast to the situation with bulk Au surfaces,[7,8] which leads to a nearly complete surface ML of Pt. This result is not completely surprising, given the vastly different geometries of 1.6 nm NP surfaces as compared to bulk surfaces. Indeed, as our calculations have shown, the flexibility of AuNPs can enable rapid AuPt alloying during HT Pt deposition, which is not accessible for comparatively rigid bulk Au.

The second important outcome is the necessity of combining well-defined experimental models (e.g., DENs), numerous physical methods (e.g., electrochemistry, TEM, EDS, and XAS), and appropriate theory to ascertain reliable structural information about such complex materials.

Finally, we point out that the present study was undertaken using just a single combination of metals (Au and Pt) and a single size of NP (1.6 nm). It is certainly possible, likely even, that application of the HT method to other metals,[13,14] as well as other NP sizes and shapes, will lead to other structures, including perhaps core@shell NPs. Additionally, we have not begun to address the issue of multiple HT iterations,[7,8,14] even for the AuPt system.

Unanswered questions remain for the AuPt NPs reported here. First, the alloy formation mechanism is still tentative and lacks experimental verification. Second, in the interest of clarity, the roles of chemical gradients and melting point depression in alloy formation were not explored. We hope to investigate these influences in future studies. Third, we previously reported the synthesis of Au@Pt DENs using UPD followed by Pt GE, but characterization of those materials was far more limited than in the present case.[34,35,36] We are presently re-examining those results, using the same battery of methods used here, to determine if differences in the synthetic methods are responsible for the structural differences or if we simply drew incorrect conclusions on the basis of insufficient characterization data. The results of these studies will be reported in due course.

ASSOCIATED CONTENT

Supporting Information

The Supporting Information is available free of charge on the ACS Publications website at DOI: 10.1021/jacs.7b12306.

UV−vis and TEM for Au_{147} DENs; evidence of self-terminating Pt deposition; CVs for the EXAFS sample; EDS for the EXAFS sample; best fits to the experimental EXAFS data; XANES spectra; simulated Au and Pt foil *k*-space spectra; simulated *k*-space spectra for the NP453 Pt cluster, NP453 shell-2, and Pt_{38} models; plots showing the effects of vibrational disorder; *R*-factors for assessing the fits to the simulated EXAFS spectra; calculated Au surface energies for bulk and NP surfaces with and without H; molecular dynamics (MD) simulations for Pt deposition on icosahedral Au_{147}; the driving force for Au surface segregation after alloying; EXAFS sample preparation; TEM of the EXAFS sample; controls for the selectivity of Pt deposition (TEM, CV); Cu UPD for the EXAFS sample; and additional EXAFS fitting considerations (PDF)

AUTHOR INFORMATION

Corresponding Authors

*anatoly.frenkel@stonybrook.edu
*henkelman@mail.utexas.edu
*crooks@cm.utexas.edu

ORCID

Nicholas Marcella: 0000-0002-2224-532X
Long Luo: 0000-0001-5771-6892
Anatoly I. Frenkel: 0000-0002-5451-1207
Graeme Henkelman: 0000-0002-0336-7153
Richard M. Crooks: 0000-0001-5186-4878

Present Address

#Department of Chemistry, Wayne State University, 5101 Cass Avenue, Detroit, Michigan 48202, United States.

Notes

The authors declare no competing financial interest.

ACKNOWLEDGMENTS

We gratefully acknowledge support from the U.S. National Science Foundation under the DMREF program (L.L., A.S.L., and R.M.C., Grant no. 1534177; A.I.F., Grant no. 1726321). A.S.L., L.L., and R.M.C. (Grant F-0032) and Z.D. and G.H. (Grant F-1841) thank the Robert A. Welch Foundation for sustained research support. N.M. acknowledges support from an SBU-BNL seed grant and Laboratory Directed Research and Development Program through LDRD 18-047 of Brookhaven National Laboratory under the U.S. Department of Energy Contract No. DE-SC0012704. We also acknowledge the support of the BL2-2 beamline of the SSRL through the Synchrotron Catalysis Consortium (U.S. Department of Energy, Office of Basic Energy Sciences, Grant no. DE-

DOI: 10.1021/jacs.7b12306
J. Am. Chem. Soc. 2018, 140, 6249−6259

SC0012335). Additionally, we thank Janis Timoshenko (Stony Brook University) for carrying out the EXAFS measurements.

REFERENCES

(1) Zhang, Y.; Hsieh, Y.-C.; Volkov, V.; Su, D.; An, W.; Si, R.; Zhu, Y.; Liu, P.; Wang, J. X.; Adzic, R. R. *ACS Catal.* **2014**, *4*, 738−742.
(2) Sasaki, K.; Naohara, H.; Cai, Y.; Choi, Y. M.; Liu, P.; Vukmirovic, M. B.; Wang, J. X.; Adzic, R. R. *Angew. Chem., Int. Ed.* **2010**, *49*, 8602−8607.
(3) Anderson, R. M.; Yancey, D. F.; Zhang, L.; Chill, S. T.; Henkelman, G.; Crooks, R. M. *Acc. Chem. Res.* **2015**, *48*, 1351−1357.
(4) Dai, Y.; Chen, S. *ACS Appl. Mater. Interfaces* **2015**, *7*, 823−829.
(5) Xie, S.; Choi, S.-I.; Lu, N.; Roling, L. T.; Herron, J. A.; Zhang, L.; Park, J.; Wang, J.; Kim, M. J.; Xie, Z.; Mavrikakis, M.; Xia, Y. *Nano Lett.* **2014**, *14*, 3570−3576.
(6) Brimaud, S.; Behm, R. J. *J. Am. Chem. Soc.* **2013**, *135*, 11716−11719.
(7) Liu, Y.; Gokcen, D.; Bertocci, U.; Moffat, T. P. *Science* **2012**, *338*, 1327−1330.
(8) Ahn, S. H.; Liu, Y.; Moffat, T. P. *ACS Catal.* **2015**, *5*, 2124−2136.
(9) Liu, Y.; Hangarter, C. M.; Garcia, D.; Moffat, T. P. *Surf. Sci.* **2015**, *631*, 141−154.
(10) Deng, Y.-J.; Tripkovic, V.; Rossmeisl, J.; Arenz, M. *ACS Catal.* **2016**, *6*, 671−676.
(11) Vanpaemel, J.; Sugiura, M.; Cuypers, D.; van der Veen, M. H.; De Gendt, S.; Vereecken, P. M. *Langmuir* **2014**, *30*, 2047−2053.
(12) Ritzert, N. L.; Moffat, T. P. *J. Phys. Chem. C* **2016**, *120*, 27478−27489.
(13) Hangarter, C. M.; Liu, Y.; Pagonis, D.; Bertocci, U.; Moffat, T. P. *J. Electrochem. Soc.* **2014**, *161*, D31−D43.
(14) Ahn, S. H.; Tan, H.; Haensch, M.; Liu, Y.; Bendersky, L. A.; Moffat, T. P. *Energy Environ. Sci.* **2015**, *8*, 3557−3562.
(15) Achari, I.; Ambrozik, S.; Dimitrov, N. *J. Phys. Chem. C* **2017**, *121*, 4404−4411.
(16) Nutariya, J.; Fayette, M.; Dimitrov, N.; Vasiljevic, N. *Electrochim. Acta* **2013**, *112*, 813−823.
(17) Wang, R.; Bertocci, U.; Tan, H.; Bendersky, L. A.; Moffat, T. P. *J. Phys. Chem. C* **2016**, *120*, 16228−16237.
(18) Wang, H.; Jiang, K.; Chen, Q.; Xie, Z.; Cai, W.-B. *Chem. Commun.* **2016**, *52*, 374−377.
(19) Jeong, H.; Kim, J. *J. Phys. Chem. C* **2016**, *120*, 24271−24278.
(20) Pang, L.; Zhang, Y.; Liu, S. *Appl. Surf. Sci.* **2017**, *407*, 386−390.
(21) Ercolano, G.; Farina, F.; Cavaliere, S.; Jones, D. J.; Roziere, J. *J. Mater. Chem. A* **2017**, *5*, 3974−3980.
(22) Myers, V. S.; Weir, M. G.; Carino, E. V.; Yancey, D. F.; Pande, S.; Crooks, R. M. *Chem. Sci.* **2011**, *2*, 1632−1646.
(23) Scott, R. W. J.; Wilson, O. M.; Crooks, R. M. *J. Phys. Chem. B* **2005**, *109*, 692−704.
(24) Yeung, L. K.; Lee, C. T.; Johnston, K. P.; Crooks, R. M. *Chem. Commun.* **2001**, 2290−2291.
(25) Zhao, M.; Sun, L.; Crooks, R. M. *J. Am. Chem. Soc.* **1998**, *120*, 4877−4878.
(26) Ye, R.; Zhukhovitskiy, A. V.; Deraedt, C. V.; Toste, F. D.; Somorjai, G. A. *Acc. Chem. Res.* **2017**, *50*, 1894−1901.
(27) Astruc, D.; Wang, D.; Deraedt, C.; Liang, L.; Ciganda, R.; Ruiz, J. *Synthesis* **2015**, *47*, 2017−2031.
(28) Bronstein, L. M.; Shifrina, Z. B. *Chem. Rev.* **2011**, *111*, 5301−5344.
(29) Cuenya, B. R. *Thin Solid Films* **2010**, *518*, 3127−3150.
(30) Ghosh Chaudhuri, R.; Paria, S. *Chem. Rev.* **2012**, *112*, 2373−2433.
(31) Bakos, I.; Szabo, S.; Pajkossy, T. *J. Solid State Electrochem.* **2011**, *15*, 2453−2459.
(32) Sasaki, K.; Naohara, H.; Choi, Y. M.; Cai, Y.; Chen, W.-F.; Liu, P.; Adzic, R. R. *Nat. Commun.* **2012**, *3*, 2124.
(33) Zhang, J.; Sasaki, K.; Sutter, E.; Adzic, R. R. *Science* **2007**, *315*, 220−222.
(34) Yancey, D. F.; Carino, E. V.; Crooks, R. M. *J. Am. Chem. Soc.* **2010**, *132*, 10988−10989.
(35) Iyyamperumal, R.; Zhang, L.; Henkelman, G.; Crooks, R. M. *J. Am. Chem. Soc.* **2013**, *135*, 5521−5524.
(36) Yancey, D. F.; Zhang, L.; Crooks, R. M.; Henkelman, G. *Chem. Sci.* **2012**, *3*, 1033−1040.
(37) Carino, E. V.; Crooks, R. M. *Langmuir* **2011**, *27*, 4227−4235.
(38) Luo, L.; Zhang, L.; Henkelman, G.; Crooks, R. M. *J. Phys. Chem. Lett.* **2015**, *6*, 2562−2568.
(39) Brankovic, S. R.; Wang, J. X.; Adzic, R. R. *Surf. Sci.* **2001**, *474*, L173.
(40) Herrero, E.; Buller, L. J.; Abruna, H. D. *Chem. Rev.* **2001**, *101*, 1897−1930.
(41) Dimitrov, N. *Electrochim. Acta* **2016**, *209*, 599−622.
(42) Fayette, M.; Liu, Y.; Bertrand, D.; Nutariya, J.; Vasiljevic, N.; Dimitrov, N. *Langmuir* **2011**, *27*, 5650−5658.
(43) Luo, L.; Zhang, L.; Duan, Z.; Lapp, A. S.; Henkelman, G.; Crooks, R. M. *ACS Nano* **2016**, *10*, 8760−8769.
(44) Kim, Y.-G.; Kim, J. Y.; Vairavapandian, D.; Stickney, J. L. *J. Phys. Chem. B* **2006**, *110*, 17998−18006.
(45) Yancey, D. F.; Chill, S. T.; Zhang, L.; Frenkel, A. I.; Henkelman, G.; Crooks, R. M. *Chem. Sci.* **2013**, *4*, 2912−2921.
(46) Kresse, G.; Furthmueller, J. *Comput. Mater. Sci.* **1996**, *6*, 15−50.
(47) Kresse, G.; Furthmueller, J. *Phys. Rev. B: Condens. Matter Mater. Phys.* **1996**, *54*, 11169.
(48) Blochl, P. E. *Phys. Rev. B: Condens. Matter Mater. Phys.* **1994**, *50*, 17953−17979.
(49) Kresse, G.; Joubert, D. *Phys. Rev. B: Condens. Matter Mater. Phys.* **1999**, *59*, 1758−1775.
(50) Perdew, J. P.; Ruzsinszky, A.; Csonka, G. I.; Vydrov, O. A.; Scuseria, G. E.; Constantin, L. A.; Zhou, X.; Burke, K. *Phys. Rev. Lett.* **2008**, *100*, 136406.
(51) Duan, Z.; Li, Y.; Timoshenko, J.; Chill, S. T.; Anderson, R. M.; Yancey, D. F.; Frenkel, A. I.; Crooks, R. M.; Henkelman, G. *Catal. Sci. Technol.* **2016**, *6*, 6879−6885.
(52) Zabinsky, S. I.; Rehr, J. J.; Ankudinov, A.; Albers, R. C.; Eller, M. J. *Phys. Rev. B: Condens. Matter Mater. Phys.* **1995**, *52*, 2995−3009.
(53) Kim, Y. G.; Oh, S.-K.; Crooks, R. M. *Chem. Mater.* **2004**, *16*, 167−172.
(54) Luo, L.; Duan, Z.; Li, H.; Kim, J.; Henkelman, G.; Crooks, R. M. *J. Am. Chem. Soc.* **2017**, *139*, 5538−5546.
(55) Carino, E. V.; Kim, H. Y.; Henkelman, G.; Crooks, R. M. *J. Am. Chem. Soc.* **2012**, *134*, 4153−4162.
(56) Machado, S. A. S.; Tanaka, A. A.; Gonzalez, E. R. *Electrochim. Acta* **1991**, *36*, 1325−1331.
(57) Frenkel, A. I. *Chem. Soc. Rev.* **2012**, *41*, 8163−8178.
(58) Menard, L. D.; Wang, Q.; Kang, J. H.; Sealey, A. J.; Girolami, G. S.; Teng, X.; Frenkel, A. I.; Nuzzo, R. G. *Phys. Rev. B: Condens. Matter Mater. Phys.* **2009**, *80*, 64111.
(59) Garcia-Gutierrez, D. I.; Gutierrez-Wing, C. E.; Giovanetti, L.; Ramallo-Lopez, J. M.; Requejo, F. G.; Jose-Yacaman, M. *J. Phys. Chem. B* **2005**, *109*, 3813−3821.
(60) Klementiev, K. V. XAFSmass, freeware: https://intranet.cells.es/Beamlines/CLAESS/software/xafsmass.html.
(61) Calvin, S. *XAFS for Everyone*; CRC Press/Taylor & Francis Group: Boca Raton, FL, 2013; pp 297−318.
(62) Zhou, S.; Jackson, G. S.; Eichhorn, B. *Adv. Funct. Mater.* **2007**, *17*, 3099−3104.
(63) Divi, S.; Chatterjee, A. *J. Phys. Chem. C* **2016**, *120*, 27296−27306.
(64) Pedersen, M. O.; Helveg, S.; Ruban, A.; Stensgaard, I.; Laegsgaard, E.; Norskov, J. K.; Besenbacher, F. *Surf. Sci.* **1999**, *426*, 395−409.
(65) Irissou, E.; Laplante, F.; Garbarino, S.; Chaker, M.; Guay, D. *J. Phys. Chem. C* **2010**, *114*, 2192−2199.
(66) Wang, D.; Liu, S.; Wang, J.; Lin, R.; Kawasaki, M.; Rus, E.; Silberstein, K. E.; Lowe, M. A.; Lin, F.; Nordlund, D.; Liu, H.; Muller, D. A.; Xin, H. L.; Abruna, H. D. *Nat. Commun.* **2016**, *7*, 11941.
(67) Weir, M. G.; Knecht, M. R.; Frenkel, A. I.; Crooks, R. M. *Langmuir* **2010**, *26*, 1137−1146.

DOI: 10.1021/jacs.7b12306
J. Am. Chem. Soc. 2018, 140, 6249−6259